Efficient synthesis of syngas from CO_2 electrochemical reduction over a dual functional Fe_xC@CNT/N-MXene catalyst

Pan-Pan Guo [a], Zhen-Hong He [a,*], Hui-Hui Cao [a], Kuan Wang [a], Weitao Wang [a], Yue Tian [a], Jiajie Liu [a], Lu Li [c,d], Zhao-Tie Liu [a,b,**]

[a] Shaanxi Key Laboratory of Chemical Additives for Industry, College of Chemistry and Chemical Engineering, Shaanxi University of Science & Technology, Xi'an 710021, China
[b] School of Chemistry & Chemical Engineering, Shaanxi Normal University, Xi'an 710119, China
[c] Key Laboratory of Auxiliary Chemistry and Technology for Chemical Industry, Ministry of Education, Shaanxi University of Science and Technology, Xi'an 710021, China
[d] Shaanxi Collaborative Innovation Center of Industrial Auxiliary Chemistry and Technology, Shaanxi University of Science and Technology, Xi'an 710021, China

ARTICLE INFO

ABSTRACT

Syngas, composed of CO and H_2, is a crucial precursor for the synthesis of hydrocarbons and aldehydes. Compared with traditional ways, the co-electrolysis of CO_2 and water represents a sustainable approach to producing syngas using CO_2 resources. In this work, we represented co-electrolysis of CO_2 and water to syngas over an Fe_xC@CNT/N-MXene catalyst in an H-type cell. The catalyst delivers tunable CO/H_2 ratios at a wide potential range from -0.8 to -1.2 V (*vs.* RHE) and provides equal FE_{CO} and FE_{H2} together with a current density of 26 mA cm^{-2} at -1.1 V (*vs.* RHE). Characterization results and DFT calculation confirmed that nanosized Fe_xC wrapped inside carbon nanotubes (CNTs) are the main active sites for CO_2ER to CO, while the N-doped $Ti_3C_2T_x$ MXenes (N-MXene) are active sites for HER. The present work provides a strategy for constructing an efficient catalyst in CO_2ER to syngas and offers a guideline for creating dual-functional catalysts in other reactions.

1. Introduction

CO_2 is a waste gas, and its high concentration in the atmosphere is one of the primary reasons for climate change. Reducing CO_2 concentration is still a big challenge at the present stage. The chemical utilization of CO_2 has emerged as an important approach to reducing CO_2 emission and producing value-added products and thus has caught much attention in the last several decades [1,2]. Typically, CO_2 electrocatalytic reduction (CO_2ER) into high-valued chemicals and fuels including HCOOH, CO, CH_4, CH_3OH, C_2H_5OH, and C_3H_7OH, *etc.* is one of the ideal ways to achieve carbon neutrality [3–8]. Syngas, a mixed gas of CO and H_2, is a feedstock for synthesizing various important chemicals *via* the Fischer-Tropsch (F-T) process, hydroformylation, carbonylation, *etc* [9–11]. Importantly, the syngas with diverse CO/H_2 molar ratios could be directly used in these reactions to produce different targets. For example, methanol, light olefins, and methane can be synthesized from syngas with H_2/CO ratios of 1/1, 2/1, and 3/1, respectively [12,13]. In this respect, producing syngas with adjustable H_2/CO molar ratios is very important and attractive.

Co-electrolysis of CO_2 and water, *i.e.*, a combination of CO_2ER and hydrogen evolution reactions (HER), can produce syngas over suitable catalysts. The route avoids shortcomings such as the requirements of high energy and cost, and operation under harsh conditions in conventional reverse water-gas shift reaction (RWGS) and steam reformation [14]. However, CO_2 is a chemically inert molecule, and its activation requires high overpotential and high energy input. To efficiently overcome these issues, developing efficient catalytic systems for co-electrolysis of CO_2 and water to syngas is one of the preferred strategies but is still a challenge. Indeed, to date, many catalysts have been well established for the reaction[15] such as Zn- [16], Ag- [17], and Cu-based[18] catalysts *via* strategies of crystal and morphology engineering, alloy engineering, and doping heteroatoms, *etc*. Although great progress has been achieved, efficient catalysts for generating syngas from CO_2 and water are still rare.

Considering the titled reaction requiring two active sites for CO_2ER and HER, the construction of a bifunctional catalyst is an ideal protocol

---

* Corresponding author.
** Corresponding author at: School of Chemistry & Chemical Engineering, Shaanxi Normal University, Xi'an 710119, China.
E-mail addresses: hezhenhong@sust.edu.cn (Z.-H. He), ztliu@snnu.edu.cn (Z.-T. Liu).

[19]. Indeed, CO_2ER to CO is a 2-proton/electron reaction and can be facilely achieved with high selectivity and activity, and it is well-studied for its high technological and economic feasibility [20,21]. Apart from the state-of-the-art Au and Ag catalysts [22,23], many catalysts are active in CO_2ER to CO, including $CuInSe_2$ with Se vacancies [24], metal-free nitrogen-doped carbon materials (mf-NCs) [25], ZnO nanosheets with oxygen vacancies [26], and porous dendritic oxide derived zinc (OD-Zn) [22], *etc.* Among these catalysts, the metal-doped nitrogenated carbon (M-N-C) derived from pyrolysis of nitrogenous organic compounds such as urea, biomass-derived materials, metal-organic frameworks (MOFs), *etc.* has received much attention for the properties of excellent stability, abundant porosity, and various functionalities [27]. Many metals loaded in carbon matrices such as Fe-N-C and Ni-N-C *etc.* could successfully catalyze the CO_2ER to CO, but not be active for HER in the same reaction cell [28]. Although similar catalysts were established, developing an M-N-C material, beneficial for the co-electrolysis of CO_2 and water to syngas is still a difficult issue.

As for HER, the primary competitive reaction to CO_2ER in an aqueous electrolyte could be also solely catalyzed by many catalysts [29]. Among them, MXenes, new two-dimensional (2D) materials, are transition metal carbides and nitrides and have attracted much attention in photocatalysis, sensing, electromagnetic shielding, supercapacitors, *etc* [30,31]. In electrocatalysis, especially in hydrogen evolution reaction (HER), oxygen reduction reaction (ORR), nitrogen reduction reaction (NRR), CO_2 reduction reaction (CO_2RR), and methanol oxidation reaction [32,33], MXene materials also presented good performances. However, MXene-based catalysts are rarely used in electrocatalytic CO_2 reduction, including the co-electrolysis of CO_2 and water to syngas. Thus, we reasonably speculate that MXenes could maintain their intrinsic activity for HER after suitable modification in CO_2 electrolysis.

Fe is a promising catalyst in CO_2ER because of its abundant reserve and low price. For instance, the catalysts such as Fe-N-C[34] and C-Fe30-N30/30[35] were developed in the reaction. Among these catalysts, the single Fe atom in Fe-N-C catalysts and Fe-N sites are always recognized as active sites to produce CO. Inspired by the activities of Fe-based catalysts and MXene materials in CO_2ER and HER, herein, we combined them to build an $Fe_xC@CNT/N$-MXene catalyst in achieving co-electrolysis of CO_2 and water to syngas. The total Faradic efficiencies of CO and H_2 (FE_{CO} and FE_{H2}) reached approximately 100% with an equal molar ratio of H_2/CO (0.97), together with a current density of 26 mA cm^{-2} at -1.1 V (*vs.* RHE). Importantly, the H_2/CO molar ratio could be adjusted from 0.22 to 2.82 by just tuning the applied potentials from -0.8 V to -1.2 V (*vs.* RHE) in 0.1 mol/L KCl electrolyte. The present catalyst showed competitive performances in comparison to the developed materials in Table S1, especially for some noble-metal catalysts. Compared with other developed Fe-based catalysts, the present Fe-based catalyst delivers higher current densities. Besides, the most reported Fe-based catalysts offer a high activity in CO_2ER to CO, but not syngas. The Fe_xC component is responsible for the single CO_2ER, while N-MXene is an active site for HER, which was confirmed by DFT calculation and the control experiments of metal poisoning by KSCN. Characterization results confirmed that the presence of CNTs could improve the textural properties and conductivity of the catalysts [36]. The present work offers an efficient $Fe_xC@CNT/N$-MXene catalyst for co-electrolysis of CO_2 and water and also develops a strategy to design and prepare dual-functional catalysts, which will offer an important reference in other coupling reactions.

2. Experimental section

2.1. Materials

Lithium fluoride (LiF, >99%, Shanghai Shaoyuan Reagent Co., Ltd.), iron (III) chloride hexahydrate ($FeCl_3$·6 H_2O, >99%, Shanghai Macleans Biochemical Technology Co., Ltd.), Toray carbon paper (CP, TGP-H-60) with measuring 1 cm × 1 cm, melamine ($C_3H_6N_6$, >99%, Shanghai

Macleans Biochemical Technology Co., Ltd.), and Nafion D-521 dispersions (5% w/w in the mixture of water and 1-propanol, ≥ 0.92 meg/g exchange capacity) are provided from commercial resources. Ti_3AlC_2 MAX (>99.5%) was provided by Shandong Xiyan New Material Technology Co., Ltd. KSCN (>98.5%) was obtained from Greagent. CO_2 and Ar (99.999%) were provided by Xi'an Teda Cryogenic Equipment Co., Ltd. All other used reagents are provided from commercial resources.

2.2. Preparation of the $Ti_3C_2T_x$ MXene

The $Ti_3C_2T_x$ MXene was obtained by etching the Al layer in Ti_3AlC_2 MAX material. Typically, LiF (1 g) was dissolved into HCl solution (9 mol/L, 20 mL) under stirring. Then, Ti_3AlC_2 MAX powder (1 g) was slowly added to the above solution to avoid overheating during the reaction. The etching was maintained for 24 h at 35 °C in an oil bath, followed by centrifugation (3500 rpm/min) and washing with water until pH > 6. The obtained powder was dispersed under sonication for 2 h, followed by centrifuging and drying at 80 °C for 24 h to obtain $Ti_3C_2T_x$ MXene.

2.3. Preparation of the $Fe_xC@CNT/N$-MXene

The $Fe_xC@CNT/N$-MXene catalyst was fabricated *via* hydrolysis of a mixture of melamine, $FeCl_3$, and $Ti_3C_2T_x$ MXene. Typically, 9 mmol $C_3H_6N_6$, 4.3 mmol $FeCl_3$·6 H_2O, and 75 mg $Ti_3C_2T_x$MXene were added to 12 mL HCl solution (1 mol/L) under stirring. After 3 h, the mixture was freeze-dried for 24 h and heated to 800 °C at 2 °C/min under N_2 flow (30 mL/min). The sample was calcined at 800 °C for 2 h, and upon calcination, the $Fe_xC@CNT/N$-MXene catalyst was obtained, where N-MXene means N-doped $Ti_3C_2T_x$. For comparison, other catalysts including $Fe_xC@CNT$, CNT/N-MXene, physically mixed $Fe_xC@CNT$, and N-MXene ($Fe_xC@CNT$ + N-MXene) were prepared with similar methods. N-doped MXene without CNTs component was also prepared by calcinating MXene under ammonia (NH_3) according to the former report [37].

2.4. Co-electrolysis of CO_2 and water to syngas

The co-electrolysis of CO_2 and water was conducted in an H-type cell by using a three-electrode system including a working electrode, a reference electrode (3 mol/L KCl, Ag/AgCl), and a Pt mesh auxiliary electrode, respectively. The catalytic performances were evaluated on an electrochemical workstation (CHI660E, Shanghai Chenhua Co., Ltd).

Generally, 3 mg catalyst, 800 μL isopropanol, and 50 μL Nafion solution (5 wt%) were mixed under ultrasonication at room temperature for 3 h to obtain a uniform ink solution. The ink was slowly dripped onto a carbon paper (1 ×1 cm^2). According to the weight of the carbon paper before and after loading a catalyst, the loading amount was determined as 0.92 mg/cm^2. Before the test, the cathode cell was treated with Ar or CO_2 gas for 40 min, and then the LSV curves were tested from -1.13 to -1.35 V (*vs.* RHE) at a scanning rate of 50 mV·s^{-1}. Ag/AgCl was used as the reference electrode. The following formula (1) can convert the potentials (*vs.* Ag/AgCl) to the values (*vs.* RHE).

$$E \ (vs \cdot RHE) = E \ (vs \cdot Ag/AgCl) + 0 \cdot 222 + 0 \cdot 059 \times pH \tag{1}$$

The reaction gas was detected by GC (GC9720Plus, Zhejiang Fuli Analytical Instrument Inc), and the electrolyte after the reaction was tested by ^{1}H NMR (Bruker Avance III 400 HD spectrometer).

2.5. Electrochemical measurements

The electrochemically active surface area (ECSA) was obtained by testing the electric double layer (C_{dl}). To obtain C_{dl}, cyclic voltammetry (CV) curves were tested from -0.2018 to 0.0018 V (*vs.* RHE) at the scan rates from 20 mV·s^{-1} to 180 mV·s^{-1} with an increase amplitude of 20 mV·s^{-1}. The relationship between the current density differences ($\Delta j =$

j_a-j_c) and scan rates was obtained, and the linear slope is twice the C_{dl}. The ECSA values (A_{ECSA}) were obtained from the C_{dl}/Cs ratio, where Cs defines the specific capacitance for a flat standard electrode with a 1 cm^2 area. Cs was 0.04 mF cm^{-2} in the present calculation.

The electrochemical impedance of the composite material reveals its influence on the electrode kinetics of the reaction. Generally, electrochemical impedance spectroscopy (EIS) is tested at open circuit voltage (OCP) with an amplitude of 10^{-2}~10^5 Hz.

2.6. Characterization

(High-resolution) transmission electron microscope ((HR)TEM) images of the catalyst were measured on TF20 (EFI, Tecnai, USA) transmission electron microscope at a 200 KV working voltage. The spherical-aberration corrected transmission electron microscope (Sc-TEM) was conducted on JEM-ARM 300 F (JEOL, Japan). X-ray photoelectron spectroscopy (XPS) spectra were recorded on AXIS SUPRA using Al Kα radiations (hν = 1486.6 eV) at 9.8×10^{-10} Torr. All the binding energies were calibrated with the C 1 s at 284.8 eV. X-ray Diffraction (XRD) patterns were conducted on a Rigaku D/max 2500 with nickel-filtered Cu Kα (λ = 0.154 nm) at 40 kV and 20 mA in the range of 5° to 80°. Raman spectra of the samples were tested on Renishaw inVia Raman Microscope. The Raman spectra were collected using a glass slide and a 532 nm laser for excitation. The *in-situ* Raman spectra were acquired in a homemade flow cell equipped with a quartz window. The device was composed of a three-electrode system. Before tests, the catalyst was fixed in the cell and the CO_2-saturated electrolyte (0.1 M KCl) was introduced into the cathode chamber and the anode chamber at a rate of 5 mL/min. The Raman spectra were recorded by exciting with a 532 nm laser under different applied potentials.

N_2 adsorption/desorption and CO_2 adsorption experiments were tested on ASAP 2460 (Micromeritics, USA). The samples (100 mg) were degassed under a vacuum of 10^{-5} torr at 200 °C for 12 h. The catalysts' surface areas were obtained according to the Brunauer-Emmett-Teller (BET) method by analyzing the relative pressures (P/P$_0$) from 0.05 to 0.3.

Temperature-programmed desorption (TPD) experiments were tested on an AUTOCHEM II 2920 (Micromeritics, USA) instrument. Before the experiments, the samples underwent a heating process in a helium gas (He) environment at a flow rate of 30 mL/min, reaching 300 °C to eliminate any adsorbed water and gas from the samples. Subsequently, the samples were cooled to 50 °C, and the gas was switched to probe molecules, namely CO_2, CO, and H_2, by using 10% CO_2/He, 10%CO/He, and 5%H_2/He gas mixtures, respectively. These gases were allowed to adsorb onto the samples for 1 h at a rate of 30 mL/min. Afterward, the gas was switched back to He to remove any remaining residual gas for another hour. Finally, the samples were heated to the set temperatures at 10 °C/min, while the desorbed gas was recorded by a thermal conductivity detector (TCD).

2.7. DFT calculations

The calculation was conducted by using the first-principles to perform all Spin-polarization density functional theory (DFT) calculations within the GGA using the PBE formulation [38]. PAW potentials were used to describe the ionic cores and took valence electrons into account using a plane wave basis set with a kinetic energy cutoff of 520 eV, as implemented in VASP [39,40]. To account for partial occupancies of the Kohn-Sham orbitals, the Gaussian smearing method with a width of 0.05 eV was used. When the energy change was smaller than 10^{-5} eV, the electronic energy was considered self-consistent. When the energy change was smaller than 0.03 eV Å^{-1}, a geometry optimization was considered convergent. During the calculations, the electronic energy was considered self-consistent when the energy change was smaller than 10^{-5} eV, and a geometry optimization was considered convergent after the energy change was smaller than 0.03 eV Å^{-1}.

In our structure, a U correction was involved for Fe atoms. For the Fe$_3$C (002) surface, the vacuum spacing was set to 18 Å. To perform the Brillouin zone integration, a $2 \times 2 \times 1$ Monkhorst-Pack k-point sampling was used for a structure. The adsorption energies (E_{ads}) were calculated by using the following formula (2):

$$E_{ads}= E_{ad/sub} - E_{ad} - E_{sub} \tag{2}$$

where $E_{ad/sub}$, E_{ad}, and E_{sub} are the total energies of the optimized adsorbate/substrate system, the adsorbate in the structure, and the clean substrate, respectively. The free energy was calculated using the equation of (3):

$$G = E_{ads}+ ZPE - TS \tag{3}$$

where G, E_{ads}, ZPE, and TS are the free energy, total energy from DFT calculations, zero point energy, and entropic contributions, respectively.

3. Results and discussion

3.1. Catalyst characterizations

The prepared samples were characterized by different technologies to discover the structural properties. Initially, the morphologies of Ti$_3$C$_2$T$_x$ MXene and the Fe$_x$C@CNT/N-MXene catalyst were tested by TEM (Figs. S1 and 1). After etching, the Ti$_3$C$_2$T$_x$ MXene exhibits a structure of few-layer nanosheets, which was confirmed by TEM images in Fig. S1 **(a-c)**. Besides, the nanosheet structure could be found on the cross-section of bending in the red cycle (Fig. S1c). The HRTEM image shows the single crystallinity of the MXene sheet (the inset of Fig. S1c) [41]. The STEM and element mappings show the Ti and C elements are well dispersed over the whole nanosheets (Fig. S1d-**f**). The EDS element mappings with raw intensity of Ti and C, and energy spectrum are also exhibited in Fig. S1, confirming the Ti and C elements are dispersed well. The Fe$_x$C@CNT/N-MXene catalyst exhibits a rather complicated structure, which shows the CNTs aggregates formed during the calcination of melamine and lamellar MXene (Fig. 1**a**). The nanoparticles, indexed to Fe$_3$C, were wrapped in the CNTs (Fig. 1**b** and **e**), and the HRTEM image shows that lattice spacings of 0.15 nm and 0.35 nm attributed to the (020) planes of Fe$_3$C and the (002) planes of CNTs (Fig. 1**c** and **f**). The HRTEM images confirmed that the Fe$_3$C nanoparticles also exist in small particles with a size of only 5 nm and the lattice spacings of 0.30 nm and 0.25 nm could be assigned to (111) and (200) planes of Fe$_3$C (Fig. 1**d**). The results indicated that the Fe$_3$C nanoparticles exist in the catalyst both in big size (45 nm) and small size (5 nm). The Sc-TEM image in Fig. 1**g** also reveals the particle wrapped in CNTs in Fig. 1**e** was Fe$_3$C, supported by the lattice spacing of 0.11 nm assigned to Fe$_3$C (152) planes. The selective area electron diffraction pattern (SAED) pattern showed diffraction rings corresponding to the (020) and (111) planes of Fe$_3$C from outside to inside (Fig. 1**h**). The diffraction spots were probably stemmed from the nanoparticles in the yellow dotted cycles around the selected area (marked by the red box) in Fig. 1**h**. The HAADF image and element mappings with raw intensity confirm that the Fe element exists both in dispersion and particles, and the other elements such as C, N, and Ti are well dispersed in the catalyst (Fig. 1**i-n**). The EDS energy spectrum of the Fe$_x$C@CNT/N-MXene is given in Fig. S2, which supports the presence of Fe, C, N, and Ti. These results showed that the Fe$_x$C@CNT/N-MXene catalyst consists of CNTs embedded in N-MXene, and CNTs are formed by pyrolysis of melamine. The CNTs and lamellar N-MXene were integrated, while Fe$_x$C nanoparticles were wrapped in CNTs. The complicated structure provides the potential for multi-functional applications.

The melamine not only acted as the precursor for CNTs, but also provided N atom to form N-doped MXene, which was proved by XPS test in Fig. 2. The C 1 s spectrum deconvoluted into five peaks could be assigned to C-C, C-N, C-O, C═O, and O-C═O species (Fig. 2**a**) [42,43]. No C-Fe peak was detected for its low concentration, confirming that
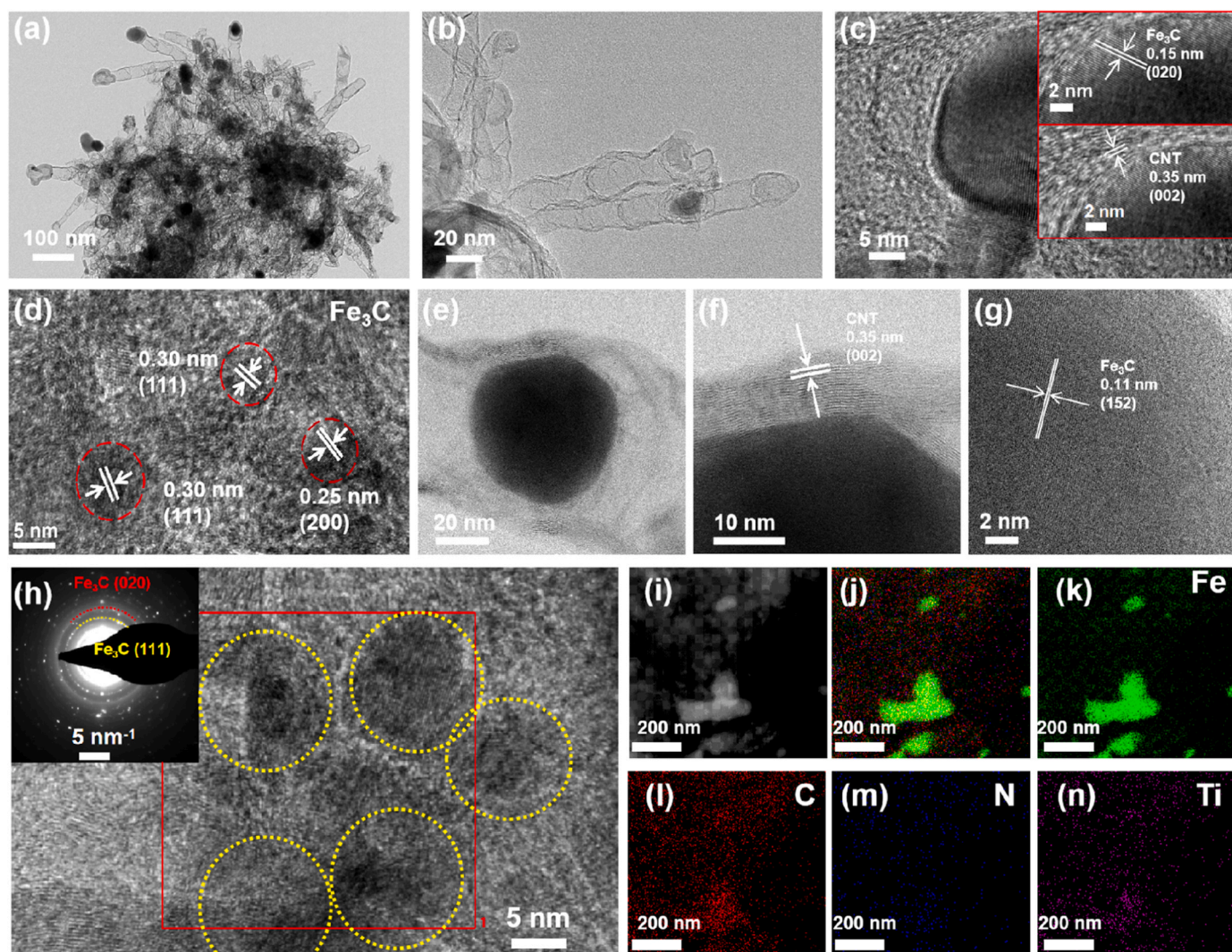
Fig. 1. (HR)TEM images (a-g), SAED pattern and selected region (h), HAADF image (i), and element mappings (j-m) of the $Fe_xC@CNT/N$-MXene catalyst, respectively.

Fe_xC was wrapped into the CNT. For comparison, we also tested the XPS of the Ti_3C_2 MXene sample with the results collected in Fig. S3. The Ti-C could be found in C1s XPS; however, neither Fe nor N element was found. The results also indirectly supported that Fe_xC species, without a Fe-C bond in Fig. 2a, were successfully wrapped in the CNT.

It is worth noting that the Fe 2p XPS signal is weak for the low Fe concentration on the catalyst surface, which is only 0.2 wt%. Compared with the Fe loading of 36% (ICP-OES results, Table S2), such a low concentration on the surface also supports that most Fe elements are wrapped into CNTs. The XPS spectrum of N 1 s confirmed that the existence of M-N (M means metal), pyridinic N, pyrrole N, and graphite N, assigned from the peaks at 395.6, 397.8, 400.9, and 402.8 eV, respectively (Fig. 2c) [43]. For the Ti 2p XPS spectrum, the fitted peaks at 455.7, 457.1, and 458.4 eV belong to the Ti $2p_{3/2}$ peaks of the Ti-C, Ti-N, and Ti-O species, respectively, while the peaks at 461.5, 462.8, and 464.1 eV could be attributed to Ti 2p1/2 peaks for Ti-C, Ti-N, and Ti-O species (Fig. 2d) [43,44]. The results confirmed that the N atom has been successfully doped on the MXene materials *via* the formations of C-N and Ti-N bonds, which is consistent with the previous report [45]. Thus, we denoted the N-doped MXene as N-MXene. The following studies reveal the CNTs were less active for the HER and CO_2ER, while the N-MXene was active for the HER.

XRD patterns were investigated to identify the bulk phase structure

of the samples, with the results given in Fig. 3a. Both MXene and N-MXene were tested, and an obvious peak appears at 7.8° indexed to the (002) planes of the $Ti_3C_2T_x$ with a *d*-spacing of 1.13 nm, indicating that the Ti_3AlC_2 MAX material has been successfully etched to MXene nanosheets [45,46]. For the $Fe_xC@CNT/N$-MXene catalyst, together with the peaks of MXene, some new peaks appeared at 37.6, 39.9, 40.6, 42.8, 43.6, 44.5, 44.9, 45.9, and 48.6°, which could be assigned to the (021), (200), (120), (121), (210), (022), (103), (211), and (113) crystal planes of Fe_3C (PDF# 06–0688), respectively [47]. The results confirmed the presence of Fe_3C species, and this is consistent with the former TEM results. Besides, the peak at 26.4° was assigned to CNT [44]. The results confirmed that the catalyst comprises Fe_xC, CNTs, and MXene components. No obvious MXene peaks particularly at low angles could be found in the $Fe_xC@CNT/N$-MXene catalyst, which was because the MXene layers were destroyed by intercalation of gas and impurities during the heat treatment of catalyst preparation, and this was confirmed by the TEM results in Fig. 1 and S1. In the TEM image of MXene, the layers could be found on the cross-section of bending in the red cycle (Fig. S1c). However, in the $Fe_xC@CNT/N$-MXene, no similar layer structure could be found (Fig. 1).

N_2 adsorption/desorption isotherms are given in Fig. 3b, and the results indicated that the $Fe_xC@CNT/N$-MXene catalyst shows a type-IV hysteresis loop, indicative of the presence of mesopores structure. The
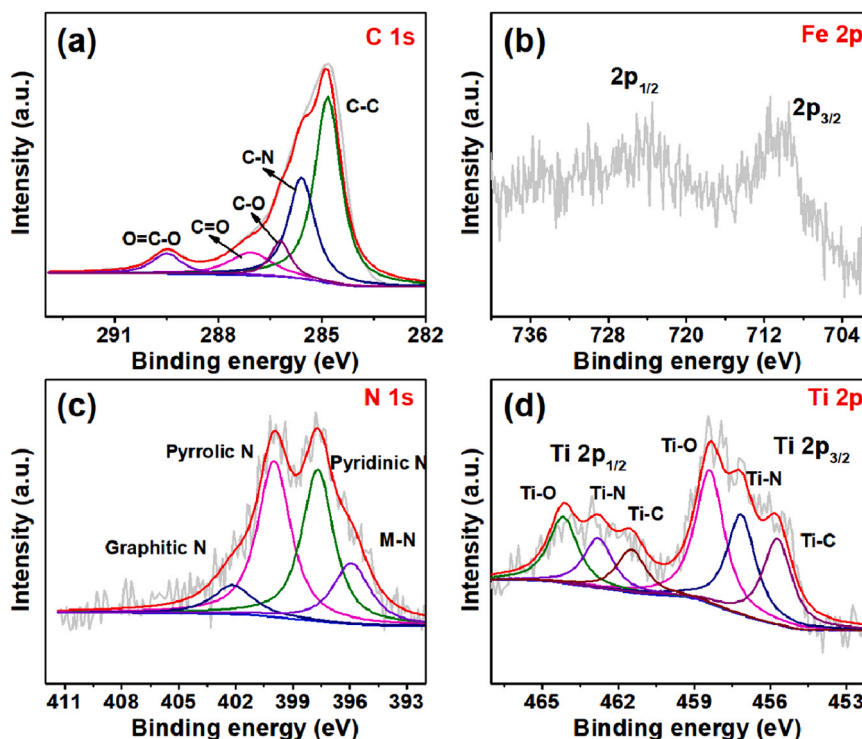
Fig. 2. XPS spectra of the C 1 s (a), Fe 2p (b), N 1 s (c), and Ti 2p (d) elements of the Fe$_x$C@CNT/N-MXene catalyst.
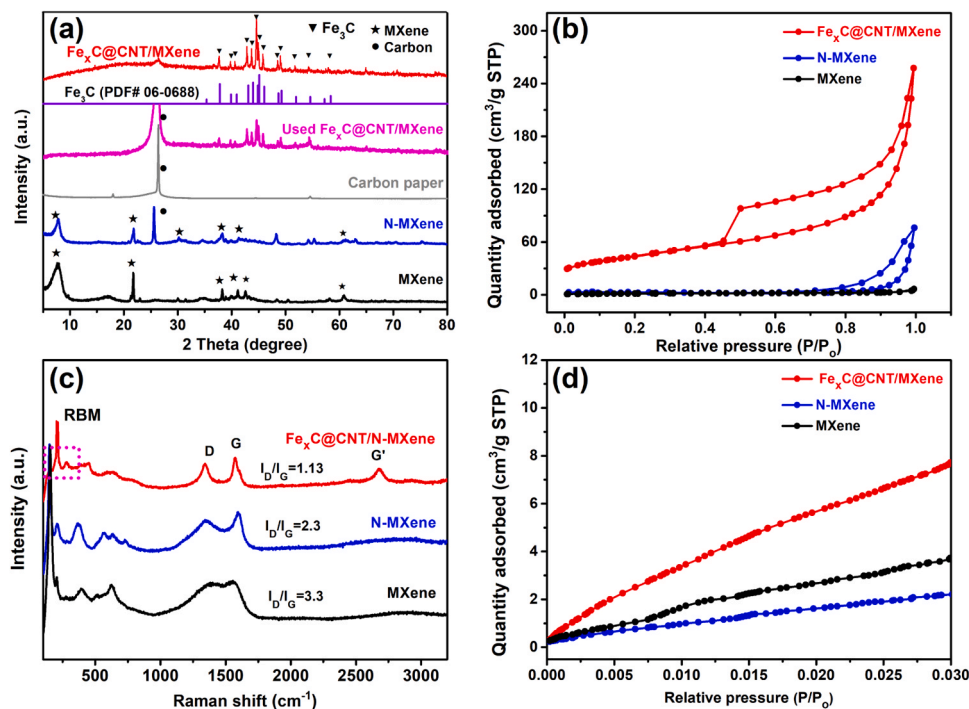

Fig. 3. XRD patterns (a), N$_2$ adsorption/desorption isotherms (b), Raman spectra (c), and CO$_2$ adsorption isotherms (d) of different samples.

CNTs act as a support for Fe$_x$C nanoparticles and could provide net structures for the catalyst. This will be beneficial for the mass transfer of gas molecules and electrolyte. The Fe$_x$C@CNT/N-MXene catalyst showed a much higher BET-specific surface area than those of MXene and N-MXene (154 *vs.* 5 and 9 m^2/g) (Table S3), which is conducive to mass transfer during the reaction.

Raman spectroscopy can evaluate the defect of carbon materials *via*

the I$_D$/I$_G$ ratio, and the I$_D$ and I$_G$ are the intensities of D and G band peaks at approximately 1350 and 1580 cm^{-1}, respectively. The I$_D$/I$_G$ ratio of the Fe$_x$C@CNT/N-MXene catalyst is 1.13, much lower than those of MXene and CNT/N-MXene, indicating that the catalyst has the highest degree of graphitization [48] since Fe species could catalyze the graphitization of carbon [49]. Besides, some new peaks appeared at 208 cm^{-1} and 2685 cm^{-1} for the Fe$_x$C@CNT/N-MXene catalyst,

attributing to the radial breathing mode (RBM) and G′ peaks of the carbon nanotubes, indicative of the CNTs formation during the preparation [50]. The G′ band (or 2D band) relates to Raman scattering of the vibration mode of carbon respiration in the hexagonal lattice of graphene [50]. The CO_2 adsorption capacities for catalysts were also measured, with the results given in Fig. 3d. The results showed that the Fe$_x$C@CNT/N-MXene catalyst has a higher CO_2 adsorption capacity than those of MXene and CNT/N-MXene, demonstrating that it probably has a super catalytic activity in the reaction.

3.2. Catalytic performances

The CO_2ER over the prepared Fe$_x$C@CNT/N-MXene catalyst was conducted in an H-type cell in a KCl aqueous solution. Initially, LSV curves were recorded from − 0.8 to − 1.2 V (*vs.* RHE), the current density obtained in CO_2-saturated KCl electrolyte is higher than that in Ar-saturated electrolyte, indicating that CO_2ER occurred under the given conditions. By contrast, the carbon paper showed a low current density in both CO_2- and Ar-saturated electrolytes, indicative of their lower electrocatalytic activities (Fig. 4a). The electrolyte plays a very important role in the electrochemical reduction of CO_2 because it co-ordinates with the reactants, intermediates, and products on the electrode surface [51,52]. The aqueous electrolyte is a promising solvent in the CO_2ER reaction for the existence of abundant protons [53], and the electrolytes containing K^+ cations are often adopted because they can accelerate the activation of CO_2 [54]. We studied the CO_2ER over the present catalyst in different K^+ salts as electrolytes to investigate their performances. Compared with the KHCO$_3$, KOH, K$_2$SO$_4$, K$_2$CO$_3$, *etc.* electrolytes, KCl aqueous solution delivers the highest performances in producing syngas with an FE$_{CO}$ of 51.1% and FE$_{H2}$ of 49.8% and n_{H2}/n_{CO} of 0.99 (Fig. S4). Other tested electrolytes, however, showed low catalytic performances since they offer a different local environment on the catalyst, especially the pH [55]. The products obtained in the CO_2ER in CO_2-saturated KCl electrolyte were mainly CO and H$_2$, which were confirmed by gas chromatography (GC) and ^{1}H NMR (Figs. S5 and S6).

The catalytic performances over the Fe$_x$C@CNT/N-MXene catalyst at different potentials are shown in Fig. 4b. At potentials lower than − 1.0 V (*vs.* RHE), CO was the main product. However, H$_2$ gradually dominated with the increase of the potential, indicating that the H$_2$/CO molar ratio could be adjusted by only changing the potential. The syngas with approximately equal FE$_{CO}$ (51.1%) and FE$_{H2}$ (49.8%) were obtained at − 1.1 V (*vs.* RHE) and the current density researched was 26 mA/cm^{-2}. Changing the applied potentials, the molar ratio of H$_2$/CO could increase from 0.22 to 2.82, which could be used in different reactions like F-T synthesis and hydroformylation, *etc.*

By comparison, the catalytic performances over the catalysts of Fe$_2$O$_3$ without CNTs or N-MXene, CNTs, and Fe$_x$C@CNT/N-MXene derived from different ratios of C$_3$H$_6$N$_6$/MXene were also investigated. The results showed that Fe$_2$O$_3$ and CNTs catalysts had little catalytic activities in the CO_2ER or HER, while the Fe$_x$C@CNT/N-MXene (1:13) had the highest activity (Fig. 4c). The CNTs were directly derived from the melamine, thus the feed of melamine affected the loadings remarkably. The Fe loading was tested to be 36 wt% *via* the ICP-OES. As mentioned above, the CNTs could improve the conductivity of the catalyst, too low or too high loading of CNTs resulted in a low activity, which was probably due to the low loading could not improve the conductivity of the catalyst, and the high loading lowers the concentration of active sites.

The MXene could catalyze the HER with a mediate FE$_{H2}$, however, no CO was detectable, indicating that it could not catalyze the CO_2ER (Fig. 4d). The total FE was less than 100%, which was due to the ohmic consumption and the charge storage caused by the double capacitance effect of the catalytic material [56]. The results indicated that CNTs are not active for HER under the given conditions, and to further confirm these results, we conducted a control experiment by using N-MXene without CNTs, which was prepared *via* nitridation by ammonia. The obtained performances are provided in Fig. S7a. Compared with the results of MXene in Fig. 4d, the N-doping MXene, *i.e.*, N-MXene could cause a reduction in FE of H$_2$, especially at low potential from − 0.8 V to − 1.0 V (*vs.* RHE). The result suggests the N-doped MXene could prevent
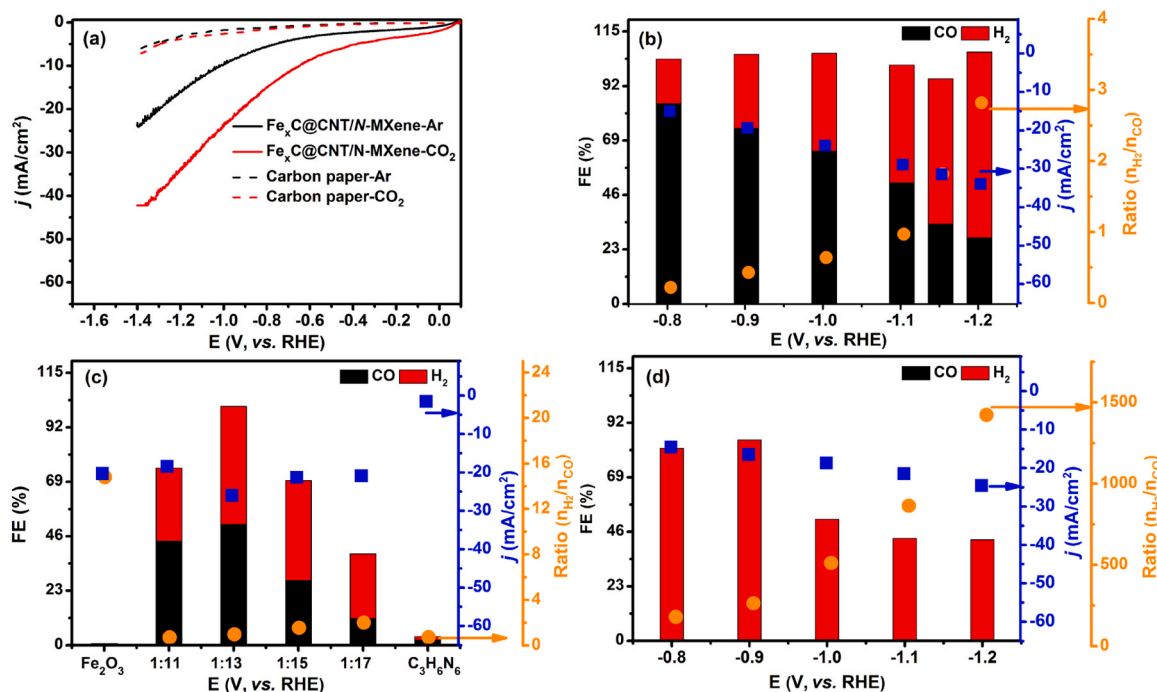

Fig. 4. (a) LSV curves of the Fe$_x$C@CNT/N-MXene catalyst and carbon paper in CO_2 and Ar saturated 0.1 mol/L KCl solution. (b) Effect of potentials on the catalytic performances of CO_2ER over the Fe$_x$C@CNT/N-MXene catalyst. (c) Catalytic performances of CO_2ER over the Fe$_2$O$_3$, the Fe$_x$C@CNT/N-MXene derived from different C$_3$H$_6$N$_6$/MXene molar ratios, and CNTs material derived from sole C$_3$H$_6$N$_6$ (1:11 refers to the molar ratio of C$_3$H$_6$N$_6$/MXene), and over (d) MXene at different potentials.

excessive hydrogen evolution reaction.

It is worth noting that the present co-electrolysis of CO_2 and water could be achieved under the microcosmic cooperation of N-MXene and Fe$_x$C@CNT in the Fe$_x$C@CNT/N-MXene catalyst. The physically mixed Fe$_x$C@CNT and N-MXene, however, could not produce enough CO, which was probably due to the poor mutual touch between them and further reducing the conductivity of the Fe$_x$C@CNT component (Fig. S7b). The results also indicated that there is probably an interaction between the Fe$_x$C@CNT and N-MXene. To verify this inference, we further studied the performances of different catalysts in chemical adsorption of CO_2, H_2, and CO, and the results are collected in Fig. 5 and S8. The CO_2-TPD curves confirm that compared with other samples, the Fe$_x$C@CNT/N-MXene catalyst with three components of Fe$_x$C, CNT, and N-MXene shows a great enhancement in CO_2 adsorption, especially at higher 300 °C, indicative of the presence of a strong interplay between the catalyst and CO_2 molecules. At the temperature range of 50–450 °C, the N-MXene component could promote CO_2 adsorption, which was probably due to the great amount of groups including -OH on the N-MXene (Fig. S8) [57]. The Fe$_x$C@CNT/N-MXene catalyst also showed the highest H_2 and CO adsorption amounts in H_2-TPD and CO-TPD at a high-temperature range. The results indicated there is a strong interaction among the Fe$_x$C, CNT, and N-MXene components. In contrast to CO, the present Fe$_x$C@CNT component could adsorb more CO_2 from 450 °C to 600 °C, indicating it has a greater potential in CO_2 conversion rather than CO conversion.

The electrochemically active surface area (ECSA) demonstrates the kinetic parameters of an electrochemical reaction over a given catalyst, and the ECSA values of the Fe$_x$C@CNT/N-MXene, physically mixed Fe$_x$C@CNT and N-MXene, N-MXene, and MXene were 33.4, 27.9, 19.3, and 21.8 mF/cm^2, respectively. The Fe$_x$C@CNT/N-MXene possesses the highest ECSA, implying that it has more active sites for the reaction (Fig. 6a). Besides, in the impedance tests, the Fe$_x$C@CNT/N-MXene exhibits the lowest radius, confirming that it possesses the highest overall electron conductivity, which is beneficial for the electrons transformation to activate CO_2 to CO_2.$^-$ intermediate (Fig. 6b) [58].

The stability of the Fe$_x$C@CNT/N-MXene catalyst was also investigated with the results given in Fig. 6c. Within 8 h, the current density of the Fe$_x$C@CNT/N-MXene slightly increased, while the FEs of CO and H_2 slightly decreased. Despite the slight change in activity, the present catalyst offered acceptable stability during the reaction. To investigate the crystal structure, morphology, and surface information, we tested the used Fe$_x$C@CNT/N-MXene *via* the SEM, (HR)TEM, XRD, XPS, Raman, *etc*. The SEM image showed the fresh catalyst shows a complicated morphology with abundant interwoven pores, which is beneficial for the mass transfer of the gas molecules and electrolyte (Fig. S9a). The used catalyst still maintained a similar morphology to the fresh one but had more and larger pores, which was probably due to the swelling of the electrolyte (Fig. S9b).

The crystalline structure of the used catalyst was tested in Fig. 3, and

the main peaks at the *2θ* from 35° to 60° could be assigned to Fe$_3$C (PDF card # 06–0688), and peak approximately 28°stemmed from the carbon paper. The results showed that Fe$_x$C species maintained well during the reaction, and the Fe$_x$C/CNT component is active for the CO_2ER to CO.

The TEM tests also confirmed the stability of the catalysts. The used catalysts still comprised CNTs, and Fe$_x$C particles, and similar to the fresh catalyst, the MXene component was not obvious appear (Fig. S10a and b). The SAED pattern also confirms the presence of Fe$_3$C species, deriving from the diffraction rings of (020) and (221) planes, and the HRTEM images show the lattice spacings of 0.24, 0.11, and 0.17 nm could be assigned to (240), (152), and (122) planes of Fe$_3$C, respectively (Fig. S10c-e). The results indicated that the present catalyst has good stability both in catalytic performances and catalytic structures, and the Fe species are in the form of Fe$_x$C.

The XPS tests of the used catalyst were also applied, and the results are collected in Fig. S11. The C, Fe, N, and Ti XPS peaks are similar to those in the fresh catalyst (Figs. S11 *vs* 2). However, the surface Fe concentration in the used catalyst was increased to 0.8% (Table S2), which was probably due to the electrolyte flushing during the reaction. The increase in current density during the long-term study was probably due to the more Fe-species exposed. However, it is very difficult to distinguish the Fe^0 and Fe$_x$C from the Fe2p XPS results for the low concentration of Fe on the catalyst.

The Raman spectrum of the used Fe$_x$C@CNT/N-MXene catalyst still shows D, G, and G′ bands and the I_D/I_G was 0.92, lower than the value of 1.13 in the fresh catalyst, which was probable due to the introduction of carbon paper components during the Raman test (Figs. S12). The results showed that CNTs and Fe$_x$C NPs still exist in the used catalysts, and the used catalyst maintained a similar structure to the fresh one. The good stability of Fe$_x$C was probably due to the protective effect of CNTs, which prevents the leaching and reduction of Fe$_x$C.

3.3. In-situ Raman tests

In-situ Raman tests for the Fe$_x$C@CNT/N-MXene catalyst in the co-electrolysis of CO_2 and water were conducted under different applied potentials, with the results and the testing setup given in Fig. 7 and S13. At the range of 200 to 500 cm^{-1}, no obvious peaks were detected, and this is probably the easy desorption of CO on the catalyst surface (Fig. 7a). Generally, the *CO was adsorbed on metal at this range [59]. At 714 and 1550 cm^{-1}, the peaks could be detected and assigned to the *COO$^-$ species, which was probably one of the intermediates for the CO_2 reduction [50,60–63]. The results confirmed that CO_2ER over the Fe$_x$C@CNT/N-MXene catalyst involved *COO$^-$ intermediate, and those results provided important information in the following DFT calculations.
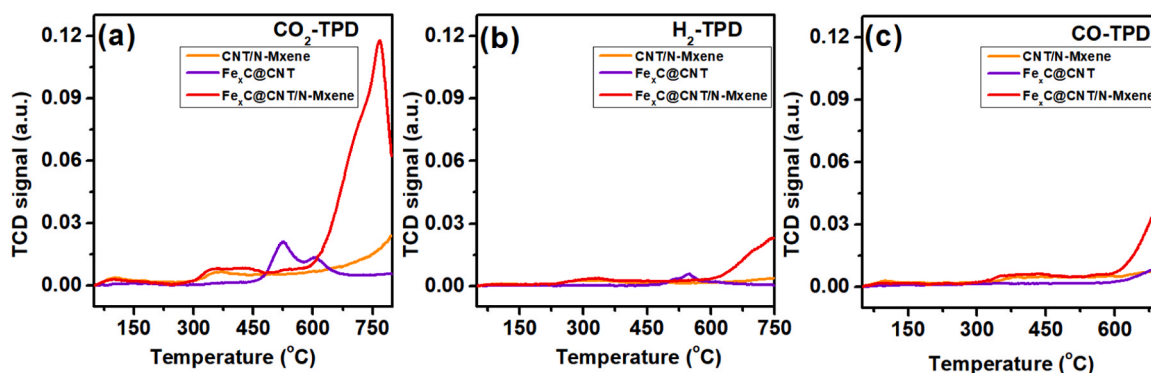

Fig. 5. CO_2-TPD (a), H_2-TPD (b), and CO-TPD (c) tests for the samples of CNT/N-MXene, Fe$_x$C@CNT, and Fe$_x$C@CNT/N-MXene, respectively.
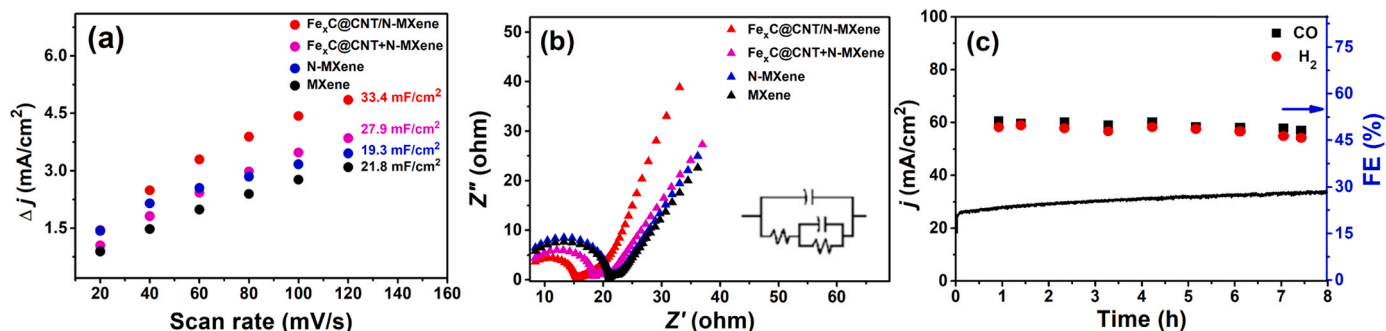
Fig. 6. The electrochemically active surface area (ECSA) (a), the electrochemical impedance (EIS) (b) of diverse samples in 0.1 mol/L KCl electrolyte, and (c) the stability of the $Fe_xC@CNT/N$-MXene at -1.1 V (*vs.* RHE), respectively.

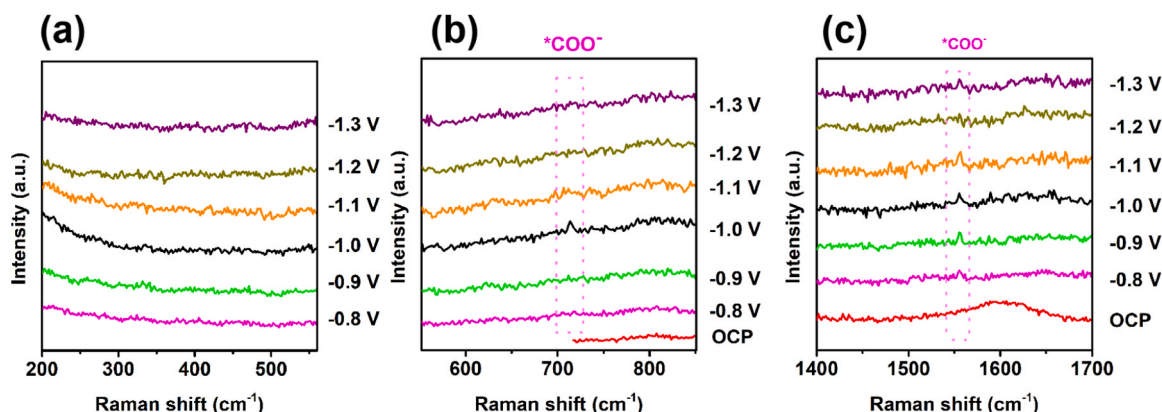**Fig. 7.** *In situ* Raman spectra for the CO_2ER over the $Fe_xC@CNT/N$-MXene catalyst at different applied potentials (a) 200 - 620 cm^{-1}, (b) 500 - 900 cm^{-1}, and (c) 1400 - 1700 cm^{-1}, respectively. Reaction conditions: 0.1 mol/L KCl electrolyte, the $Fe_xC@CNT/N$-MXene catalyst, tested potentials from -0.8 V to -1.3 V (*vs.* RHE).

3.4. Poisoning experiments and the active sites for the $Fe_xC@CNT/N$-MXene catalyst

To discover the active sites for the $Fe_xC@CNT/N$-MXene catalyst, we conducted control experiments to investigate the catalytic activities of CO_2ER and HER over different catalysts. The catalytic performances of the $Fe_xC@CNT$ catalysts in CO_2-saturated electrolytes are shown in Fig S14. As shown in Fig. S14, FE_{CO} is much higher than FE_{H2} from -0.8 to -1.1 V (*vs.* RHE), indicating that the $Fe_xC@CNT$ component contributes to CO_2ER. Therefore, we speculated that $Fe_xC@CNT$ is the active site for CO_2ER and HER, respectively.

It is well known that thiocyanate anions (SCN⁻) are capable of poisoning metals such as Fe, Co, Cu, *etc.* by forming stable metal-ligand complexes, further resulting in their deactivation [64,65]. To avoid the high concentration of SCN⁻ which prevents CO_2 from approaching the catalyst surface, we added very small amounts of KSCN (0.0075 and 0.05 mol/L) into 0.1 M KCl electrolyte to evaluate the catalytic performances (Fig. S15). Compared with the results in Fig. 4b, the reaction in (KSCN + KCl) electrolytes showed a low activity in CO formation, showing that the Fe_xC activity was restrained and the Fe_xC is the real active role of CO_2 reduction. However, the FE_{H2} of N-MXene is slightly affected by adding SCN⁻, indicative of the inertness of Ti towards SCN⁻[66]. These results confirmed that Fe_xC and N-MXene are the active sites for CO_2ER and HER, respectively.

3.5. Reaction mechanism

To discover the active sites of the $Fe_xC@CNT/N$-MXene catalyst, DFT calculations were conducted. Theoretical models of the catalyst were first constructed based on the former characterization results and

previous reports [67]. Top and side views of the optimized configurations for $Fe_3C@CNT$ and N-MXene are given in Fig. 8a-d, and activation processes of CO_2 on the $Fe_3C@CNT$ and H_2O on the N-MXene are exhibited in Fig. 8e-h, respectively. Generally, the mechanism of CO_2ER to CO involves two steps, *i.e.*, CO_2 is initially adsorbed on the catalyst to conduct a proton-coupled electron transfer process to form a *COOH intermediate ($CO_2 + H^+ + e^- \rightarrow$ *COOH), which was confirmed by the above *in-situ* Raman spectra. Following that, the *COOH intermediate is reduced to *CO through electron-proton transfer and then desorbed from the electrode [21] (*COOH $+ H^+ + e^- \rightarrow$ *CO $+ H_2O$). The main pathways for HER involve $H_2O \rightarrow$ *$H_2O \rightarrow$ *OH-H $\rightarrow$ *OH + *H and *H^+ $+ 2e^- \rightarrow 1/2$ H_2 (Fig. 8i).

In the present catalyst, of the CO_2ER reaction, the free energies of *COOH and *CO on the $Fe_xC@CNT$ are 0.53 eV and 0.10 eV, which are lower than those on the N-MXene sites (0.76 eV for *COOH, and 0.10 eV for *CO, respectively), indicating that $Fe_3C@CNT$ is more likely to generate CO, further confirming that Fe_xC is the active site of CO_2ER. As for HER reaction, the free energies of *OH-H, *OH+ *H, and *H on N-MXene are lower than those on $Fe_xC@CNT$, indicating that the N-MXene is prone to H_2 generation, which further confirms that the N site is the HER active site.

According to the above studies on characterizations, catalytic performances, and DFT calculations, we speculate that the roles of Fe_xC, CNT, and N-MXene in achieving CO_2 electrolytic reduction to syngas are as follows. The Fe_xC, wrapped in CNT, is the main active site for CO_2 reduction to CO. The structure of Fe_xC wrapped in CNT could prevent the Fe_xC from leaching and reducing during the reaction, and thus the catalyst shows acceptable stability. In addition, the CNT could provide a spatial network structure for the catalyst, and thus, offer a high BET and abundant pores for mass transfers of gas molecules and electrolyte. The
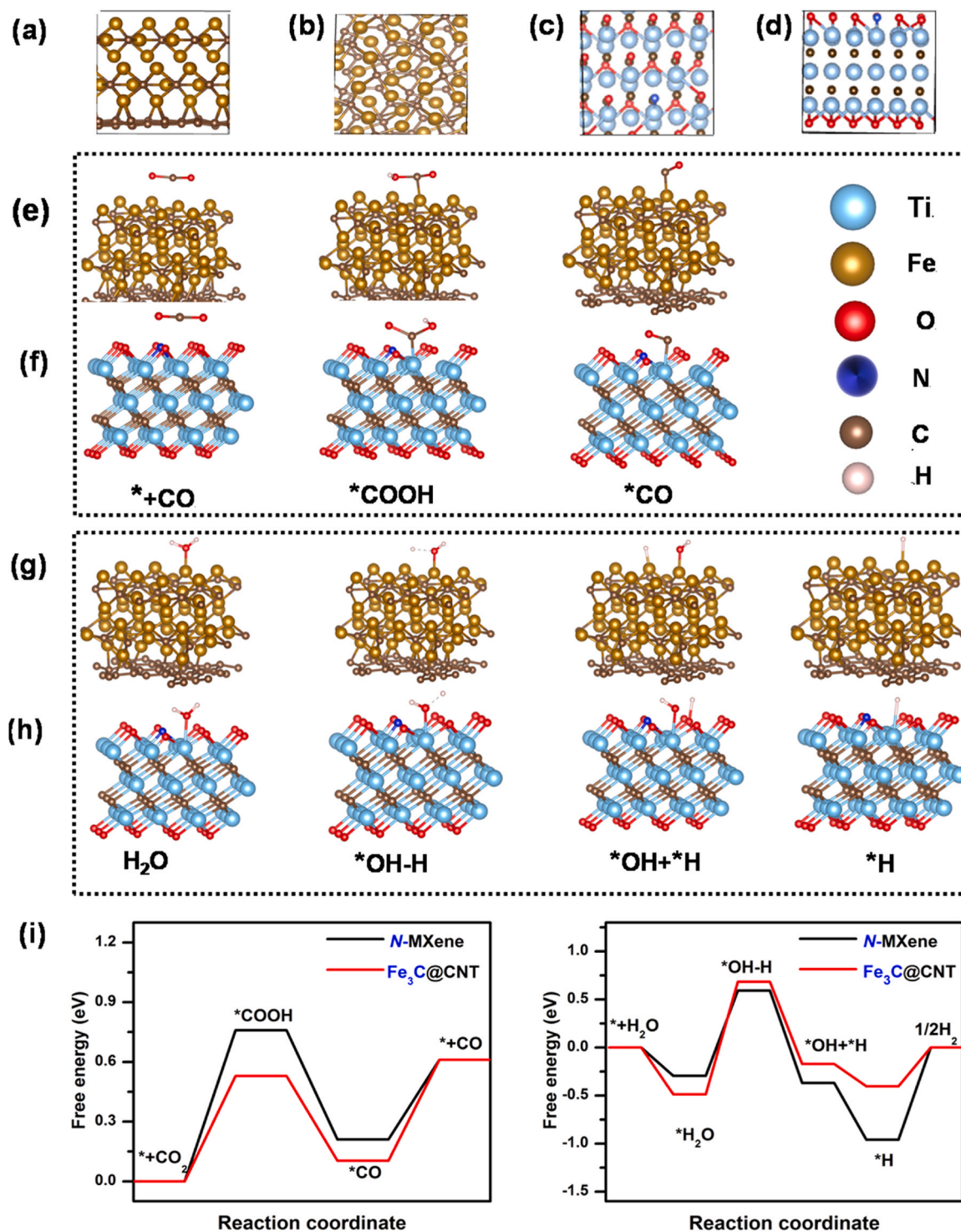
Fig. 8. Top and side views of the Fe$_3$C@CNT (a, b) and N-MXene catalyst (c, d), CO$_2$ activations on Fe$_3$C@CNT (e) and N-MXene (f), H$_2$O activations on Fe$_3$C@CNT and N-MXene (g, h), and the free energy diagrams of CO$_2$ER and HER on the Fe$_3$C@CNT and N-MXene (i).

N-MXene component could promote CO$_2$ adsorption on the catalyst, and the results are similar to the DFT calculation. Although these components individually play important roles, it is worth mentioning that the combination of them could deliver excellent performance in CO$_2$ER to syngas, confirming the presence of strong interaction among them.

4. Conclusion

The Fe$_x$C@CNT/N-MXene catalyst was prepared by the pyrolysis method, which was applied in catalyzing co-electrolysis of CO$_2$ and water to the syngas of CO and H$_2$. The syngas with different molar ratios of H$_2$/CO could be produced only by adjusting the applied potentials. Among them, an equal composition of CO and H$_2$ was obtained at a potential of − 1.1 V (*vs.* RHE), which could be used directly in reactions such as hydroformylation and FT synthesis. Characterization results confirmed that Fe$_x$C, carbon nanotubes, and N-doped MXene are formed during the preparation process. Fe$_x$C and N-MXene are supported to the active sites for CO$_2$ER to CO and HER to H$_2$, respectively, which was

proved by poisoning experiments by SCN⁻ and DFT calculations. The present work provided an efficient catalyst for the co-electrolysis of CO_2ER and HER to syngas, and this strategy would be expected to design other dual functional catalysts for coupling reactions like co-electrolytic CO_2ER and HER.

CRediT authorship contribution statement

Pan-Pan Guo: Data curation, Writing – original draft. **Zhen-Hong He:** Conceptualization, Methodology, Writing – original draft, Investigation. **Hui-Hui Cao:** Data curation, Software, Formal analysis. **Kuan Wang:** Data curation, Software. **Weitao Wang:** Conceptualization, Visualization. **Yue Tian:** Formal analysis, Conceptualization. **Jiajie Liu:** Methodology. **Lu Li:** Conceptualization, Methodology. **Zhao-Tie Liu:** Funding acquisition, Supervision, Writing – review & editing.

Declaration of Competing Interest

The authors declare that they have no known competing financial interests or personal relationships that could have appeared to influence the work reported in this paper.

Data Availability

Data will be made available on request.

Acknowledgments

Appendix A. Supporting information

Supplementary data associated with this article can be found in the online version at doi:10.1016/j.apcatb.2024.123786.

References

[1] Y. Sun, M. He, B. Han, Green carbon science: efficient carbon resource processing, utilization, and recycling towards, carbon neutrality, Angew. Chem. Int. Ed. 61 (2021) e202112835, https://doi.org/10.1002/anie.202112835.
[2] S. Khalili, A. Afkhami, T. Madrakian, Electrochemical simultaneous treatment approach: electro-reduction of CO₂ at Pt/PANI@ZnO paired with wastewater electro-oxidation over PbO₂, Appl. Catal. B-Environ. 328 (2023) 122545, https://doi.org/10.1016/j.apcatb.2023.122545.
[3] Y.-X. Duan, Y.-T. Zhou, Z. Yu, D.-X. Liu, Z. Wen, J.-M. Yan, Q. Jiang, Boosting production of HCOOH from CO₂ electroreduction via Bi/CeOₓ, Angew. Chem. Int. Ed. 60 (2021) 8798–8802, https://doi.org/10.1002/anie.202015713.
[4] M. Ma, Z. Zheng, W. Yan, C. Hu, B. Seger, Rigorous evalution of liquid products in high-rate CO₂/CO electrolysis, ACS Energy Lett. 7 (2022) 2595–2601, https://doi.org/10.1002/anie.202015713.
[5] L. Qin, L. Gao, H. Wu, X. Li, K. Qi, Q. Yi, J. Zhang, L. Shi, Fabrication of Cu(100) facet-enhanced ionic liquid/copper hybrid catalysis via one-step electro-codeposition for CO₂ER toward C₂, Fuel 322 (2022) 124103, https://doi.org/10.1016/j.fuel.2022.124103.
[6] Z. Jiang, Y. Wu, X. Lu, Y. Liang, H. Wang, Domino electroreduction of CO₂ to methanol on a molecular catalyst, Nature 575 (2019) 639–642, https://doi.org/10.1038/s41586-019-1760-8.
[7] C.-C. Chang, S.-C. Lin, S.-Y. Chiu, H.-T. Pai, T.-Y. Liao, C.-S. Hsu, W.-H. Chiang, M.-K. Tsai, H.M. Chen, Operando time-resolved X-ray absorption spectroscopy reveals the chemical nature enabling highly selective CO₂ reduction, Nat. Commun. 11 (2020) 3525, https://doi.org/10.1038/s41467-020-17231-3.
[8] F. Li, Y.C. Li, Z. Wang, J. Li, D.-H. Nam, Y. Lum, M. Luo, X. Wang, A. Ozden, S.-F. Hung, B. Chen, Y. Wang, J. Wicks, Y. Xu, Y. Li, C.M. Gabardo, C.-T. Dinh, Y. Wang, T.-T. Zhuang, D. Sinton, E.H. Sargent, Cooperative CO₂-to-ethanol

[9] conversion via enriched intermediates at molecule-metal catalyst interfaces, Nat. Catal. 3 (2019) 75–82, https://doi.org/10.1038/s41929-019-0383-7.
D. Yang, Q. Zhu, X. Sun, C. Chen, W. Guo, G. Yang, B. Han, Electrosynthesis of defective indium selenide with 3D structure on substrate for tunable CO₂ electroreduction to syngas, Angew. Chem. Int. Ed. 59 (2020) 2354–2359, https://doi.org/10.1002/anie.201914831.
[10] B.M. Tackett, Ji.H. Lee, J.G. Chen, Electrochemical conversion of CO₂ to syngas with palladium-based electrocatalysts, Acc. Chem. Res. 53 (2020) 1535–1544, https://doi.org/10.1021/acs.accounts.0c00277.
[11] Y. Shi, S. Lu, N. Meng, S. Lu, Y. Yu, B. Zhang, Electrosynthesis of syngas via the co-reduction of CO₂ and H₂O, Cell Rep. Phys. Sci. 1 (2020) 100237, https://doi.org/10.1016/j.xcrp.2020.100237.
[12] B. Qin, Q. Zhang, Y.-H. Li, G. Yang, F. Peng, Formation of lattice-dislocated zinc oxide via anodic corrosion for electrocatalytic CO₂ reduction to syngas with a potential-dependent CO:H₂ ratio, ACS Appl. Mater. Interfaces 12 (2020) 30466–30473, https://doi.org/10.1021/acsami.0c08066.
[13] S. Guo, S. Zhao, X. Wu, H. Li, Y. Zhou, C. Zhu, N. Yang, X. Jiang, J. Gao, L. Bai, Y. Liu, Y. Lifshitz, S.-T. Lee, Z. Kang, A Co₃O₄-CDots-C₃N₄ three component electrocatalyst design concept for efficient and tunable CO₂ reduction to syngas, Nat. Commun. 8 (2017) 1828, https://doi.org/10.1038/s41467-017-01893-7.
[14] S.-Q. Li, H.-X. Liu, W.-W. Wang, W.-Z. Yu, W.-J. Zhang, C. Ma, C.-J. Jia, Partially sintered copper-ceria as excellent catalyst for the high-temperature reverse water gas shift reaction, Nat. Commun. 13 (2022) 867, https://doi.org/10.1038/s41467-022-28476-5.
[15] J.H. Lee, S. Kattel, Z. Jiang, Z. Xie, S. Yao, B.M. Tackett, W. Xu, N.S. Marinkovic, J.G. Chen, Tuning the activity and selectivity of electroreduction of CO₂ to synthesis gas using bimetallic catalysts, Nat. Commun. 10 (2019) 3724, https://doi.org/10.1038/s41467-019-11352-0.
[16] B. Qin, Y. Li, H. Fu, H. Wang, S. Chen, Z. Liu, F. Peng, Electrochemical reduction of CO₂ into tunable syngas production by regulating the crystal facets of earth-abundant Zn catalyst, ACS Appl. Mater. Interfaces 10 (2018) 20530–20539, https://doi.org/10.1021/acsami.8b04809.
[17] M. Cho, J.-W. Seo, J.T. Song, J.-Y. Lee, J. Oh, Silver nanowire/carbon sheet composites for electrochemical syngas generation with tunable H₂/CO ratios, ACS Omega 2 (2017) 3441–3446, https://doi.org/10.1021/acsomega.7b00846.
[18] Y. Wang, C. Niu, Y. Zhu, D. He, W. Huang, Tunable syngas formation from electrochemical CO₂ reduction on copper nanowire arrays, ACS Appl. Energy Mater. 3 (2020) 9841–9847, https://doi.org/10.1021/acsaem.0c01504.
[19] S. Lamaison, D. Wakerley, D. Montero, G. Rousse, D. Taverna, D. Giaume, D. Mercier, J. Blanchard, H.N. Tran, M. Fontecave, V. Mougel, Zn-Cu alloy nanofoams as efficient catalysts for the reduction of CO₂ to syngas mixtures with a potential-independent H₂/CO ratio, ChemSusChem 12 (2019) 511–517, https://doi.org/10.1002/cssc.201802287.
[20] Z. Hao, S. Jin, K. Zhang, Z. Yan, J. Chen, Advances and challenges for the electrochemical reduction of CO₂ to CO: from fundamentals to industrialization, Angew. Chem. Int. Ed. 60 (2021) 20627–20648, https://doi.org/10.1002/anie.202101818.
[21] K. Jiang, T. Zheng, H. Wang, Recent advances in electrochemical CO₂-to-CO conversion on heterogeneous catalysts, Adv. Mater. (2018) 1802066, https://doi.org/10.1002/adma.201802066.
[22] M.J. Kolb, M.P.L. Kang, F. Calle-Vallejo, B.S. Yeo, The role of undercoordinated sites on zinc electrodes for CO₂ reduction to CO, Adv. Funct. Mater. 32 (2022) 2111597, https://doi.org/10.1002/adfm.202111597.
[23] S. Choe, Y.S. Ham, M.J. Kim, T. Lim, S.-K. Kim, J.J. Kim, Electrodeposited Ag catalysts for the electrochemical reduction of CO₂ to CO, Appl. Catal. B-Environ. 208 (2017) 35–43, https://doi.org/10.1016/j.apcatb.2017.02.040.
[24] X. Zheng, J. Wang, G. Wang, Y. Cao, W. Ding, J. Zhang, H. Wu, J. Ding, H. Hu, X. Han, T. Ma, Y. Deng, W. Hu, Defective bimetallic selenides for selective CO₂ electroreduction to CO, Adv. Mater. 34 (2022) 2106354, https://doi.org/10.1002/adma.202106354.
[25] Y. Wu, C. Liu, J. Fang, K. Yu, H. Li, W. He, W.-C. Cheong, S. Liu, Z. Chen, J. Dong, C. Chen, Synergetic effect of nitrogen-doped carbon catalysts for high-efficiency electrochemical CO₂ reduction, Chin. J. Catal. 43 (2022) 1697–1702, https://doi.org/10.1016/S1872-2067(21)64006-8.
[26] X. Kong, Z. Geng, W. Chen, H. Su, Y. Liu, F. Cai, G. Wang, J. Zeng, Oxygen vacancies in ZnO nanosheets enhance CO₂ electrochemical reduction to CO, Angew. Chem. Int. Ed. 57 (2018) 6054–6059, https://doi.org/10.1002/anie.201711255.
[27] J. Xu, B. Zhang, J. Song, H. Wu, X. Mei, K. Zhang, W. Han, W. Wu, M. He, B. Han, Nanoparticles and single atoms of cobalt synergistically enabled low-temperature reductive amination of carbonyl compounds, Chem. Sci. 13 (2022) 9047–9055, https://doi.org/10.1039/D2SC01596J.
[28] W. Ju, S. Vijay, S. Bruckner, S.-C. Tsang, P. Strasser, K. Chan, Unified mechanistic understanding of CO₂ reduction to CO on transition metal and single atom catalysts, Nat. Catal. 4 (2021) 1024–1031, https://doi.org/10.1038/s41929-021-00705-y.
[29] H. Hu, J. Zhu, P. Zhao, L.Y.S. Lee, K.-Y. Wong, Recent advances in electrocatalytic hydrogen evolution using nanoparticles, Chem. Rev. 120 (2020) 851–918, https://doi.org/10.1021/acs.chemrev.9b00248.
[30] Z. Wu, C. Li, Z. Li, K. Feng, M. Cai, D. Zhang, S. Wang, M. Chu, C. Zhang, J. Shen, Z. Huang, Y. Xiao, G.A. Ozin, X. Zhang, L. He, Niobium and titanium carbides (MXenes) as superior photothermal supports for CO₂ photocatalysis, ACS Nano 15 (2021) 5696–5705, https://doi.org/10.1021/acsnano.1c00990.
[31] L. Ding, L. Wei, L. Li, T. Zhang, H. Wang, J. Xue, L. Ding, S. Wang, J. Caro, Y. Gogotsi, MXene molecular sieving membranes for highly efficient gas

separation, Nat. Commun. 9 (2018) 155, https://doi.org/10.1038/s41467-017-02529-6.

[32] J. Deng, W. Kong, L. Li, Recent advances in noble metal MXene-based catalysts for electrocatalysts, J. Mater. Chem. A 10 (2022) 14674–14691, https://doi.org/10.1039/D2TA00613H.

[33] Z. Li, N.H. Attanayake, J.L. Blackburn, E.M. Miller, Carbon dioxide and nitrogen reduction reactions using 2D transition metal dichalcogenide (TMDC) and carbide/nitride (MXene) catalysts, Energ. Environ. Sci. 14 (2021) 6242–6286, https://doi.org/10.1039/D1EE03211A.

[34] W. Ju, A. Bagger, X.L. Wang, Y.L. Tsai, F. Luo, T. Möller, H. Wang, J. Rossmeisl, A. S. Varela, P. Strasser, Unraveling mechanistic reaction pathways of the electrochemical CO_2 reduction on Fe-N-C single-site catalysts, ACS Energy Lett. 4 (2019) 1663–1671, https://doi.org/10.1021/acsenergylett.9b01049.

[35] Y. Ye, C. Yan, L. Lin, H. Wu, Q. Jiang, G. Wang, Improving CO_2 electroreduction over ZIF-derived carbon doped with Fe-N sites by an additional ammonia treatment, Catal. Today 330 (2019) 252–258, https://doi.org/10.1016/j.cattod.2018.03.062.

[36] M. Wang, L. Chen, T.-C. Lau, M. Robert, A hybrid Co quaterpyridine complex/carbon nanotube catalytic material for CO_2 reduction in water, Angew. Chem. Int. Ed. 57 (2018) 7769–7773, https://doi.org/10.1002/anie.201802792.

[37] Q. Jiang, J. Ma, Y. Zhou, W. Chu, S. Perathoner, C. Jiang, K.-H. Wu, G. Centi, Y. Liu, Tuning the chemical properties of Co–$Ti_3C_2T_x$ MXene materials for catalytic CO_2 reduction, Small (2021) 2007509, https://doi.org/10.1002/smll.202007509.

[38] J. Perdew, K. Burke, M. Ernzerhof, Generalized gradient approximation made simple, Phys. Rev. Lett. 77 (1996) 3865, https://doi.org/10.1103/physrevlett.77.3865.

[39] G. Kresse, D. Joubert, From ultrasoft pseudopotentials to the projector augmented-wave method, Phys. Rev. B 59 (1999) 1758, https://doi.org/10.1103/PhysRevB.59.1758.

[40] G. Kresse, J. Furthmüller, Efficient iterative schemes for *ab initio* total-energy calculations using a plane-wave basis set, Phys. Rev. B 54 (1996) 11169, https://doi.org/10.1103/physrevb.54.11169.

[41] R. Li, L. Zhang, L. Shi, P. Wang, MXene Ti_3C_2: an effective 2D light-to-heat conversion material, ACS Nano 11 (2017) 3752–3759, https://doi.org/10.1021/acsnano.6b08415.

[42] C. Hu, C. Yu, M. Li, X. Wang, Q. Dong, G. Wang, J. Qiu, Nitrogen-doped carbon dots decorated on graphene: a novel all-carbon hybrid electrocatalyst for enhanced oxygen reduction reaction, Chem. Commun. 16 (2015) 3419–3422, https://doi.org/10.1039/C4CC08735F.

[43] V. Natu, M. Benchakar, C. Canaff, A. Habrioux, S. Célérier, M.W. Barsoum, A critical analysis of the X-ray photoelectron spectra of $Ti_3C_2T_z$ MXenes, Matter 4 (2021) 1224–1251, https://doi.org/10.1016/j.matt.2021.01.015.

[44] J. Wang, Z. Zhang, X. Yan, S. Zhang, Z. Wu, Z. Zhuang, W.-Q. Han, Rational design of porous N-Ti_3C_2 MXene@CNT microspheres for high cycling stability in Li–S battery, Nano-Micro Lett. 12 (2019) 4, https://doi.org/10.1007/s40820-019-0341-6.

[45] X.F. Chen, Y.Z. Zhu, M. Zhang, J.Y. Sui, W.C. Peng, Y. Li, G.L. Zhang, F.B. Zhang, X. B. Fan, N-butyllithium-treated $Ti_3C_2T_x$ MXene with excellent pseudocapacitor performance, ACS Nano 13 (2019) 9449–9456, https://doi.org/10.1021/acsnano.9b04301.

[46] X. Xie, N. Zhang, Z.-R. Tang, M. Anpo, Y.-J. Xu, $Ti_3C_2T_x$ MXene as a Janus cocatalyst for concurrent promoted photoactivity and inhibited photocorrosion, Appl. Catal. B-Environ. 237 (2018) 43–49, https://doi.org/10.1016/j.apcatb.2018.05.070, 9449-9456.

[47] D.-J. Liu, M.-M. Weng, X.-Q. He, T. Asefa, Fe_3C nanoparticles-loaded 3D nanoporous N-doped carbon: a highly efficient electrocatalyst for oxygen reduction in alkaline media, Int. J. Hydrog. Energy 44 (2019) 21506–21517, https://doi.org/10.1016/j.ijhydene.2019.06.062.

[48] Z. Qiao, S. Hwang, Xing Li, C. Wang, W. Samarakoon, S. Karakalos, D. Li, M. Chen, Y. He, M. Wang, Z. Liu, G. Wang, H. Zhou, Z. Feng, D. Su, J.S. Spendelow, G. Wu, 3D porous graphitic nanocarbon for enhancing the performance and durability of Pt catalysts: a balance between graphitization and hierarchical porosity, Energy Environ. Sci. 12 (2019) 2830–2841, https://doi.org/10.1039/C9EE01899A.

[49] J. Ramirez-Rico, R.D. Hunter, Z. Schnepp, Iron-catalyzed graphitization for the synthesis of nanostructured graphitic carbons, J. Mater. Chem. A 10 (2022) 4489–4516, https://doi.org/10.1039/D1TA09654K.

[50] A. Jorio, R. Saito, Raman spectroscopy for carbon nanotube applications, J. Appl. Phys. 129 (2021) 021102, https://doi.org/10.1063/5.0030809.

[51] R. Daiyan, R. Chen, P. Kumar, N.M. Bedford, J. Qu, J.M. Cairney, X. Lu, R. Amal, Tunable syngas production through CO_2 electroreduction on cobalt-carbon composite electrocatalyst, ACS Appl. Mater. Interfaces 12 (2020) 9307–9315, https://doi.org/10.1021/acsami.9b21216.

[52] A.V. Rudnev, D.V. Vasilyev, P. Broekmann, P.J. Dyson, A general and facile approach for the electrochemical reduction of carbon dioxide inspired by deep eutectic solvents, ChemSusChem 12 (2019) 1635–1639, https://doi.org/10.1002/cssc.201900579.

[53] X. Sun, X. Tan, B. Han, Ionic liquid-based electrolytes for CO_2 electroreduction and CO_2 electroorganic transformation, Nat. Sci. Rev. 9 (2022) nwab022, https://doi.org/10.1093/nsr/nwab022.

[54] M. Huang, B. Deng, X. Zhao, S. Mou, F. Dong, Interfacial electrolyte effects on electrocatalytic CO_2 reduction, ACS Catal. 12 (2022) 331–362, https://doi.org/10.1021/acscatal.1c03501.

[55] B. Deng, M. Huang, X. Zhao, S. Mou, F. Dong, Interfacial electrolyte effects on eectrocatalytic CO_2 reduction, ACS Catal. 12 (2022) 331–362, https://doi.org/10.1021/acscatal.1c03501.

[56] S. Gao, Y. Lin, X. Jiao, Y. Sun, Q. Luo, W. Zhang, D. Li, J. Yang, Y. Xie, Partially oxidized atomic cobalt layers for carbon dioxide electroreduction to liquid fuel, Nature 529 (2016) 68–71, https://doi.org/10.1038/nature16455.

[57] B. Anasori, M.R. Lukatskaya, Y. Gogotsi, 2D metal carbides and nitrides (MXenes) for energy storage, Nat. Rev. Mater. 2 (2017), https://doi.org/10.1038/natrevmats.2016.98, 16098–11114.

[58] X. Sun, L. Lu, Q. Zhu, C. Wu, D. Yang, C. Chen, B. Han, MoP nanoparticles supported on indium-doped porous carbon: outstanding catalysts for highly efficient CO_2 electroreduction, Angew. Chem. Int. Ed. 57 (2018) 2427–2431, https://doi.org/10.1002/anie.201712221.

[59] W. Shan, R. Liu, H. Zhao, Z. He, Y. Lai, S. Li, G. He, J. Liu, Spectroscopic evidence on the origin of selectivity in CO_2 electrocatalytic reduction, ACS Nano 14 (2020) 11363–11372, https://doi.org/10.1021/acsnano.0c03534.

[60] J.-F. Li, Y.-F. Huang, S. Duan, R. Pang, D.-Y. Wu, B. Ren, X. Xu, Z.-Q. Tian, SERS and DFT study of water on metal cathodes of silver, gold and platinum nanoparticles, Phys. Chem. Chem. Phys. 12 (2010) 2493–2502, https://doi.org/10.1039/B919266B.

[61] Z.-H. He, C.-C. Li, S.-Y. Yang, J. Liu, H.-H. Cao, K. Wang, W. Wang, Y. Yang, Z.-T. Liu, Electrocatalytic CO_2 reduction to ethylene over CuO_x boosting CO_2 adsorption by lanthanide neodymium, Catal. Sci. Technol. 13 (2023) 6675–6684, https://doi.org/10.1039/D3CY00893B.

[62] Y. Xie, X. Li, Y. Wang, B. Li, L. Yang, N. Zhao, M. Liu, X. Wang, Y. Yu, J.M. Liu, Reaction mechanisms for reduction of CO_2 to CO on monolayer MoS_2, Appl. Surf. Sci. 499 (2020) 143964, https://doi.org/10.1016/j.apsusc.2019.143964.

[63] W. Wu, Q. Zhang, X. Wang, C. Han, X. Shao, Y. Wang, J. Liu, Z. Li, X. Lu, M. Wu, Enhancing selective photooxidation through Co–N_x-doped carbon materials as singlet oxygen photosensitizers, ACS Catal. 7 (2017) 7267–7273, https://doi.org/10.1021/acscatal.7b01671.

[64] P.-P. Guo, Z.-H. He, S.-Y. Yang, W. Wang, K. Wang, C.-C. Li, Y.-Y. Wei, Z.-T. Liu, B. Han, Electrocatalytic CO_2 reduction to ethylene over ZrO_2/Cu-Cu_2O catalysts in aqueous electrolytes, Green. Chem. 24 (2022) 1527–1533, https://doi.org/10.1039/D1GC04284J.

[65] R. Mercado, C. Wahl, J. En Lu, T. Zhang, B. Lu, P. Zhang, J.Q. Lu, A.L. Allen, J. Z. Zhang, S. Chen, Nitrogen-doped porous carbon cages for electrocatalytic reduction of oxygen: enhanced performance with iron and cobalt dual metal centers, ChemCatChem 12 (2020) 3230–3239, https://doi.org/10.1002/cctc.201902324.

[66] Kosohin, O. Makohoniuk, A. Kushmyruk, Electrochemical oxidation of thiocyanate on metal oxide electrodes, Mater. Today.: Proc. 6 (2019) 219–226, https://doi.org/10.1016/j.algal.2017.06.012.

[67] M. Riegraf, M.P. Hoerlein, R. Costa, G. Schiller, K. Andreas Friedrich, Sulfur poisoning of electrochemical reformate conversion on nickel/gadolinium-doped ceria electrodes, ACS Catal. 7 (2017) 7760–7771, https://doi.org/10.1021/acscatal.7b02177.